Science

RESEARCH ARTICLES

Cite as: C. Downs *et al.*, *Science* 10.1126/science.adq0872 (2025).

A near-real-time data-assimilative model of the solar corona

Cooper Downs[1]†, Jon A. Linker[1]*†, Ronald M. Caplan[1], Emily I. Mason[1], Pete Riley[1], Ryder Davidson[1], Andres Reyes[1], Erika Palmerio[1], Roberto Lionello[1], James Turtle[1], Michal Ben-Nun[1], Miko M. Stulajter[1], Viacheslav S. Titov[1], Tibor Török[1], Lisa A. Upton[2], Raphael Attie[3,4], Bibhuti K. Jha[2], Charles N. Arge[3], Carl J. Henney[5], Gherardo Valori[6], Hanna Strecker[7,8], Daniele Calchetti[6], Dietmar Germerott[6], Johann Hirzberger[6], David Orozco Suárez[7,8], Julian Blanco Rodríguez[8,9], Sami K. Solanki[6], Xin Cheng[10], Sizhe Wu[10]

[1]Predictive Science Inc., San Diego, CA, USA. [2]Southwest Research Institute, Boulder, CO, USA. [3]NASA Goddard Space Flight Center, Greenbelt, MD, USA. [4]Physics and Astronomy Department, George Mason University, Fairfax, VA, USA. [5]Space Vehicles Directorate, Air Force Research Laboratory, Kirtland Air Force Base, NM, USA. [6]Max Planck Institute for Solar System Research, Göttingen, Germany. [7]Instituto de Astrofísica de Andalucía, Consejo Superior de Investigaciones Científicas, Granada, Spain. [8]Spanish Space Solar Physics Consortium, Spain. [9]Escola Tecnica Superior d'Enginyeria, Universitat de Valencia, Paterna-Valencia, Spain. [10]School of Astronomy and Space Science, Nanjing University, Nanjing, Jiangsu, China.

***Corresponding author. E-mail: linkerj@predsci.com**

†These authors contributed equally to this work.

The Sun's corona is its tenuous outer atmosphere of hot plasma, which is difficult to observe. Most models of the corona extrapolate its magnetic field from that measured on the photosphere (the Sun's optical surface) over a full 27-day solar rotational period, providing a time-stationary approximation. We present a model of the corona that evolves continuously in time, by assimilating photospheric magnetic field observations as they become available. This approach reproduces dynamical features that do not appear in time-stationary models. We used the model to predict coronal structure during the total solar eclipse of 8 April 2024 near the maximum of the solar activity cycle. There is better agreement between the model predictions and eclipse observations in coronal regions located above recently assimilated photospheric data.

The solar corona is a hot, tenuous plasma that expands outward to become the solar wind (*1*). The corona exhibits a structure on a wide range of spatial scales and evolves dynamically on timescales that range from seconds to weeks. The solar magnetic field provides the energy that drives solar flares and coronal mass ejections (CMEs) (*2*), determines the structure of the corona and solar wind (*3*), and directs the propagation of solar energetic particles (SEPs) (*4*).

The corona is difficult to observe because of its low density and proximity to the much brighter photosphere. Observations of the corona in visible (white) light require a coronagraph (on the ground or in space) or can be taken during a total solar eclipse. Eclipses provide opportunities to observe detailed coronal structure that is not accessible to coronagraph observations (*5*). The detailed structure of the corona is determined by the magnetic field (*B*). There are few measurements of the magnetic field in the corona, but it is routinely measured in the photosphere.

Coronal magnetohydrodynamic (MHD) models use boundary conditions derived from observed photospheric fields to extrapolate the field into the corona and produce synthetic observables, such as the scattered white light that would be observed during an eclipse (*6*). Most models use a single global map of the photospheric magnetic field as their boundary condition, which provides a time-stationary approximation of the average state of the corona gathered over a solar rotation of 27 days (*7*, *8*). However, the solar corona evolves more rapidly than this, in response to the changing photospheric field (*9*–*11*).

A total solar eclipse occurred on 8 April 2024, visible across parts of Mexico, the United States, and Canada. This was near the maximum of the 11-year solar activity cycle, when we expect the photospheric magnetic field, and therefore the corona, to evolve rapidly, making a time-stationary approximation problematic. To predict the coronal structure that would be observed during this eclipse, we developed an MHD model that evolves in time, using data assimilation to provide near-real-time synthetic observables.

A near-real-time coronal model

We constructed a time-dependent model of the corona that responds to changes in photospheric magnetic fields. As input for the model, we used observations of the photospheric magnetic field, which are typically only available for the near side of the Sun, in the form of solar magnetograms (*12*). Full-Sun maps of the radial magnetic field (B_r) are required to determine the boundary conditions for the MHD model. To represent the regions that were not directly observed, we adopted a surface flux transport model (SFT) (*13*–*15*), which simulates the transport and dispersal of flux across the solar surface (*14*). We used an assimilative SFT (*14*) to ingest the magnetograms, from which it produces a continuous

approximation of the state of the photospheric B_r. The SFT produced a sequence of maps of B_r over the entire Sun.

To simulate the coronal structure and dynamics, we constructed a near-real-time predictive model that acquires magnetograms from public data sources, assimilates them into an SFT, and determines boundary conditions for a time-dependent MHD model of the solar corona. The MHD model simulates the plasma and magnetic field properties of the corona. Synthetic observables and diagnostics were calculated from the MHD model and output as a continuously updated prediction of coronal structure. The output synthetic observables include white light scattered from the coronal plasma and emission from the corona in extreme ultraviolet (EUV), visible, infrared, and x-rays. The output diagnostics are the magnetic structure and topology.

The modeling pipeline is illustrated schematically in fig. S1. To run this model in real-time requires that all steps in the processing and modeling chain (including the computationally intensive MHD model) are executed at a faster cadence than the data are acquired, which was hourly for our adopted photospheric observations. We incorporated a contingency time (5 to 10 hours) to accommodate any delays that occur at any stages of the pipeline. We refer to the output as the near-real-time state of the corona because they predict the coronal conditions a few hours before the posting of the results to our website.

Assimilation, surface flux transport, and boundary conditions

The input observations of the photospheric magnetic field were taken from the Helioseismic and Magnetic Imager (HMI) (*12*) on the Solar Dynamics Observatory (SDO) (*16*) spacecraft, which views the near side of the Sun. We adopted the HMI 720-s line-of-sight (LOS) near-real-time magnetograms at a 1-hour cadence, beginning on 16 March 2024. We supplemented these data with additional observations from the Polarimetric and Helioseismic Imager (PHI) (*17*) on the Solar Orbiter (SolO) spacecraft, which views the Sun from a different angle. From 16 March 2024 to 28 March 2024, SolO was close to the Sun-Earth line and offered no advantages over HMI data (*14*). We incorporated low-latency LOS measurements from PHI on 1 April 2024 and vector measurements from 1 April and 4 April 2024 (*14*). The PHI magnetograms were obtained with the Full Disk Telescope (FDT), which provides maps of the solar disk visible from SolO (*18*).

Both the HMI and PHI data were mapped to a latitude-longitude grid in the Carrington reference frame (*19*) and used to derive B_r (*14*). During assimilation, we weighted the HMI data by μ^4 (where $\mu = \cos\theta_d$, and θ_d is the angular distance from the center of the solar disk) and discarded those with $\mu < 0.1$. PHI data were assimilated only in a specific region and were unweighted by μ (*14*).

An example of the mapped HMI data, acquired on 2 April 2024 at 09:58 Universal Time (UT), is shown in Fig. 1A. Regions with stronger magnetic field are active regions (ARs). Assimilation occurs primarily inside the $\mu = 0.5$ contour, which we refer to as the assimilation window. A specific AR complex is visible in Fig. 1A, at the edge of the HMI field of view. This AR was located at the disk center for HMI on 26 March 2024 and exhibited additional flux emergence from 31 March to 2 April 2024, outside the HMI assimilation window. In Fig. 1B, we show B_r from PHI vector data at nearly the same time as that in Fig. 1A. The AR is close to the disk center in the PHI observation. The HMI data after assimilation weights have been applied are shown in Fig. 1C; if only HMI data were used, the AR would not be included in the assimilation. The corresponding PHI data assimilation is shown in Fig. 1D.

The data were assimilated into the High-performance Flux Transport (HipFT) model software (*14*, *15*). HipFT simulates the evolution of the photospheric B_r by assuming that it is passively transported and dispersed by processes in the dense photosphere, across the entire solar surface (*14*). The resulting B_r global map from HipFT after data assimilation is shown in Fig. 1E. These maps were used (*14*) to produce a time-evolving boundary condition for the MHD simulations (Fig. 1F).

The scalar B_r we used provides no information about the magnetic shear or twist, which stores additional energy in the magnetic field. Solar observations have shown evidence of shear and twist (*20*), especially along magnetic polarity inversion lines (PILs) and in ARs. Prominences (referred to as filaments when observed on the disk) are supported, and thermally isolated, by these fields (*21*, *22*). This energization of the magnetic field can structurally change the shape of the overlying streamers and the connectivity of the underlying fields. Previous coronal eclipse predictions have included this effect in a single boundary map (*6*). For this time-evolving simulation, we automatically identified PILs in B_r and introduced shear by applying time-dependent electric fields at the boundary (*14*).

Time-evolving MHD model

To predict the structure of the corona, we used the Magnetohydrodynamic Algorithm Outside a Sphere (Mas) code (*6*). The MHD simulation calculates the three-dimensional (3D) plasma density, temperature, vector velocity, and vector magnetic field as a function of time (*14*). From these simulation variables, we calculated synthetic observables for direct comparison with observations: visible light scattered off of coronal plasma, as observed in white light images; visible and infrared line emission, as observed during eclipse totality; and EUV and x-ray emission, as observed by spacecraft.

We drove the model with sequences of B_r boundary maps that represent the evolution of magnetic flux on the entire

solar surface. Self-consistently incorporating the boundary B_r evolution requires deriving the electric fields, which is generally not fully constrained (*23*–*26*). Previous work used a technique that drives a full thermodynamic MHD model with B_r boundary sequences (*27*). That work used a sequence of maps from an idealized but statistically solar-like SFT (*28*) to reduce data artifacts. They modeled a low-activity time period near solar minimum when a time-stationary approximation should be most applicable but still found that the time-dependent behavior differed from that of time-stationary (*29*). We extended that approach in three ways: (i) We assimilated measured photospheric magnetic fields into the model, (ii) we studied a highly active period near solar maximum; and (iii) we included the energization of the field in the boundary conditions.

The MHD simulation was started on 16 March 2024 (*14*). Continually updated predictions were posted online (*30*). The web pages provided visualizations and movies of the simulated observables, with downloadable image data. We ran the model for 32 days and 7 hours, terminating on 17 April 2024 at 19:00 UT.

Simulated behavior of the solar corona

In Fig. 2 and movies S4 to S9, we show synthetic observables (*14*) output from the simulation, which predicted the appearance to three instruments: the SDO Atmospheric Imaging Assembly (AIA), in multiple filters; the Solar Terrestrial Relations Observatory (STEREO) Coronagraph Imager-2 (COR2); and the Solar and Heliospheric Observatory (SOHO) Large Angle and Spectrometric Coronagraph (LASCO) (*14*). They show dynamical phenomena in the time-evolving simulation that would not appear in a time-stationary model, including thermal nonequilibrium (Fig. 2A) (*31*, *32*), dynamic evolution of coronal hole (CH) boundaries (Fig. 2A) (*33*), and cool plasma dynamics that occur at magnetic nulls ($|B| = 0$) above pseudostreamers (Fig. 2B) (*34*) and in filament channel formation (Fig. 2C). In Fig. 2C, we also show the magnetic squashing factor Q, a measure of the connectivity and structure of the magnetic field (*35*, *36*). The volume-rendered Q, a visualization of this structure (*6*), shows the evolution of the field. Emission lines in the visible spectrum, observed during eclipses (*37*, *38*), trace the dynamic evolution of multithermal structures (*14*) within coronal streamers (Fig. 2D). Streamer blobs (*9*), small-scale eruptions, and CMEs occur throughout the simulated time period, visible in the synthetic coronagraph images and movies (Fig. 2, E and F, and movies S8 and S9), as we expected for the real Sun during this phase of the activity cycle. Similar eruptions occurred in previous magnetic models (*39*, *40*) that did not calculate the plasma properties required to create synthetic observables.

These dynamic phenomena result from the combination of photospheric field evolution and energization of the magnetic field; time-stationary states (*14*) are less energized (fig. S7). Because we used an ad hoc approximation of the energization process, these features do not correspond to real events that occur at a given time. Nevertheless, they resemble real coronal events.

The simulated large-scale corona also shows substantial evolution over days and weeks, which caused the prediction for the corona visible on eclipse day to change over time. In Fig. 3, we show the evolution of the predicted coronal brightness and volume-rendered Q. The brightness drops by orders of magnitude with increasing distance from the Sun, so we radially detrended the simulated brightness (*14*), similarly to techniques used for analog eclipse photography (*41*). The volume-rendered Q (*6*) emphasizes finer-scale details in the magnetic field. The predicted structure of the corona changes substantially (Fig. 3) in response to changes in the photospheric field. For example, the predictions for a near-equatorial streamer on the east limb changed orientation and shape over 2 weeks, and the predicted position of a southwestern streamer changed substantially.

In a previous prediction of the 21 August 2017 eclipse (*6*), the last data used as input were taken 10 days before the eclipse. That eclipse occurred during the solar cycle's less active, declining phase, and the early coronal prediction adequately captured many features observed on eclipse day (*6*). Comparing our predictions at 10 days and 0 days before the 2024 eclipse, we found that our assimilative model predicted markedly different coronal structures. These changes would not have been captured with the previous approach.

In our assimilative model, the prediction responds to the evolution of the photospheric magnetic field, but the resulting coronal structure strongly depends on the observer's view of the photosphere. Most observations have been confined to the Sun-Earth line. Flux emergence that is not directly visible is not detected until the associated ARs rotate into view, which could be up to 18 days later. The SolO data were taken away from the Sun-Earth line and allowed us to investigate how magnetic flux emergence that is not directly visible from Earth can affect coronal structure. The emerging AR observable in Fig. 1 was visible in the PHI data but not the HMI data. This AR initiated the formation of a bright, coherent structure that replaced a more diffuse configuration (fig. S2).

Comparison with an eclipse image

In Fig. 4, we compare the model prediction from about 10 hours before totality (Fig. 4A) with a processed image taken during the eclipse (Fig. 4B) and synthetic observables 1 week later (Fig. 4C). The eclipse photo has been heavily processed (*14*). For comparison, we processed the model outputs using a wavelet-based algorithm (*42*) to approximate the sharpening applied to the observation.

Both the model predictions and the observations exhibit a highly complex corona, with multiple overlapping coronal streamers and discrete plasma structures. Some of these features are reproduced in the model, but others are not. The surface magnetic field beneath the east limb changed considerably in the 3 weeks before totality (Fig. 4, D and E). This region was visible to HMI from 16 March to 22 March 2024 but was not viewed again by either HMI or PHI before eclipse day. Although it had not yet rotated into view, flux emergence on the far side of the Sun influenced the appearance of the corona on 8 April 2024, altering the position of the bright East-limb streamer (compare Fig. 4, A and B). As the simulation continued after the eclipse, these features were incorporated over the following days, causing the East limb streamer in the model to move poleward (compare Fig. 4, A and C). The results demonstrate that the east limb structures are sensitively dependent on the incomplete underlying photospheric data. We also found discrepancies between the observation and model prediction near the poles, where the field is poorly observed.

Advantages and limitations of assimilative modeling

Our near-real-time model of the solar corona was run for 32 days leading up to and after the total solar eclipse on 8 April 2024. The model predictions changed within days, owing to solar activity (Figs. 3 and 4). We found that the simulated corona, continually driven by assimilation of photospheric data, is intrinsically different from a time-stationary one, exhibiting dynamical, solar-like phenomena. The time-evolutionary approach is akin to terrestrial weather modeling, in which a simulated state of the atmosphere is continually updated with assimilated data (*43*). It also offers computational advantages (*14*).

Our model predictions were sensitive to the availability of photospheric magnetic field observations taken away from the Sun-Earth line. Assimilation of an AR that was only visible in the PHI data modified the predicted coronal structure in its vicinity, and incorporation of additional ARs as they rotated into view after the eclipse substantially modified streamer positions. We suggest that the limited availability of that data is the largest source of discrepancies between the model and observations.

REFERENCES AND NOTES

1. S. R. Cranmer, A. R. Winebarger, The properties of the solar corona and its connection to the solar wind. *Annu. Rev. Astron. Astrophys.* **57**, 157–187 (2019). doi:10.1146/annurev-astro-091918-104416
2. T. G. Forbes, A review on the genesis of coronal mass ejections. *J. Geophys. Res.* **105** (A10), 23153–23165 (2000). doi:10.1029/2000JA000005
3. T. Wiegelmann, G. J. D. Petrie, P. Riley, Coronal magnetic field models. *Space Sci. Rev.* **210**, 249–274 (2017). doi:10.1007/s11214-015-0178-3
4. M. Desai, J. Giacalone, Large gradual solar energetic particle events. *Living Rev. Sol. Phys.* **13**, 3 (2016). doi:10.1007/s41116-016-0002-5 Medline
5. J. M. Pasachoff, V. Rušin, M. Druckmüller, P. Aniol, M. Saniga, M. Minarovjech, The 2008 August 1 eclipse solar-minimum corona unraveled. *Astrophys. J.* **702**, 1297–1308 (2009). doi:10.1088/0004-637X/702/2/1297
6. Z. Mikić, C. Downs, J. A. Linker, R. M. Caplan, D. H. Mackay, L. A. Upton, P. Riley, R. Lionello, T. Török, V. S. Titov, J. Wijaya, M. Druckmüller, J. M. Pasachoff, W. Carlos, Predicting the corona for the 21 August 2017 total solar eclipse. *Nat. Astron.* **2**, 913–921 (2018). doi:10.1038/s41550-018-0562-5
7. J. A. Linker *et al*., Magnetohydrodynamic modeling of the solar corona during Whole Sun Month. *J. Geophys. Res.* **104**, 9809–9830 (1999). doi:10.1029/1998JA900159
8. R. Lionello, J. A. Linker, Z. Mikić, Multispectral emission of the Sun during the first whole Sun month: Magnetohydrodynamic simulations. *Astrophys. J.* **690**, 902–912 (2009). doi:10.1088/0004-637X/690/1/902
9. A. P. Rouillard *et al*., Intermittent release of transients in the slow solar wind: 1. Remote sensing observations. *J. Geophys. Res. Space Phys.* **115**, 4103 (2010).
10. L. Kepko, N. M. Viall, S. K. Antiochos, S. T. Lepri, J. C. Kasper, M. Weberg, Implications of L1 observations for slow solar wind formation by solar reconnection. *Geophys. Res. Lett.* **43**, 4089–4097 (2016). doi:10.1002/2016GL068607
11. L. P. Chitta, D. B. Seaton, C. Downs, C. E. DeForest, A. K. Higginson, Direct observations of a complex coronal web driving highly structured slow solar wind. *Nat. Astron.* **7**, 133–141 (2023). doi:10.1038/s41550-022-01834-5
12. P. H. Scherrer, J. Schou, R. I. Bush, A. G. Kosovichev, R. S. Bogart, J. T. Hoeksema, Y. Liu, T. L. Duvall Jr., J. Zhao, A. M. Title, C. J. Schrijver, T. D. Tarbell, S. Tomczyk, The Helioseismic and Magnetic Imager (HMI) investigation for the Solar Dynamics Observatory (SDO). *Sol. Phys.* **275**, 207–227 (2012). doi:10.1007/s11207-011-9834-2
13. A. R. Yeates, M. C. M. Cheung, J. Jiang, K. Petrovay, Y.-M. Wang, Surface flux transport on the Sun. *Space Sci. Rev.* **219**, 31 (2023). doi:10.1007/s11214-023-00978-8
14. Materials and methods are available as supplementary materials.
15. R. M. Caplan, M. M. Stulajter, J. A. Linker, C. Downs, L. A. Upton, B. K. Jha, R. Attie, C. N. Arge, C. J. Henney, Open-source Flux Transport (OFT). I. HipFT–High-performance flux transport. *Astrophys. J. Suppl. Ser.* **278** (Suppl.), 24 (2025). doi:10.3847/1538-4365/adc080
16. W. D. Pesnell, B. J. Thompson, P. C. Chamberlin, The Solar Dynamics Observatory (SDO). *Sol. Phys.* **275**, 3–15 (2012). doi:10.1007/s11207-011-9841-3
17. S. K. Solanki, J. C. del Toro Iniesta, J. Woch, A. Gandorfer, J. Hirzberger, A. Alvarez-Herrero, T. Appourchaux, V. Martínez Pillet, I. Pérez-Grande, E. Sanchis Kilders, W. Schmidt, J. M. Gómez Cama, H. Michalik, W. Deutsch, G. Fernandez-Rico, B. Grauf, L. Gizon, K. Heerlein, M. Kolleck, A. Lagg, R. Meller, R. Müller, U. Schühle, J. Staub, K. Albert, M. Alvarez Copano, U. Beckmann, J. Bischoff, D. Busse, R. Enge, S. Frahm, D. Germerott, L. Guerrero, B. Löptien, T. Meierdierks, D. Oberdorfer, I. Papagiannaki, S. Ramanath, J. Schou, S. Werner, D. Yang, A. Zerr, M. Bergmann, J. Bochmann, J. Heinrichs, S. Meyer, M. Monecke, M.-F. Müller, M. Sperling, D. Álvarez García, B. Aparicio, M. Balaguer Jiménez, L. R. Bellot Rubio, J. P. Cobos Carracosa, F. Girela, D. Hernández Expósito, M. Herranz, P. Labrousse, A. López Jiménez, D. Orozco Suárez, J. L. Ramos, J. Barandiarán, L. Bastide, C. Campuzano, M. Cebollero, B. Dávila, A. Fernández-Medina, P. García Parejo, D. Garranzo-García, H. Laguna, J. A. Martín, R. Navarro, A. Núñez Peral, M. Royo, A. Sánchez, M. Silva-López, I. Vera, J. Villanueva, J.-J. Fourmond, C. R. de Galarreta, M. Bouzit, V. Hervier, J. C. Le Clec'h, N. Szwec, M. Chaigneau, V. Buttice, C. Dominguez-Tagle, A. Philippon, P. Boumier, R. Le Cocguen, G. Baranjuk, A. Bell, T. Berkefeld, J. Baumgartner, F. Heidecke, T. Maue, E. Nakai, T. Scheiffelen, M. Sigwarth, D. Soltau, R. Volkmer, J. Blanco Rodríguez, V. Domingo, A. Ferreres Sabater, J. L. Gasent Blesa, P. Rodríguez Martínez, D. Osorno Caudel, J. Bosch, A. Casas, M. Carmona, A. Herms, D. Roma, G. Alonso, A. Gómez-Sanjuan, J. Piqueras, I. Torralbo, B. Fiethe, Y. Guan, T. Lange, H. Michel, J. A. Bonet, S. Fahmy, D. Müller, I. Zouganelis, The Polarimetric and Helioseismic Imager on Solar Orbiter. *Astron. Astrophys.* **642**, A11 (2020). doi:10.1051/0004-6361/201935325
18. S. K. Solanki, *SO/PHI–Polarimetric and Helioseismic Imager on Solar Orbiter* (European Space Agency, 2024) , accessed 4 May 2024; https://doi.org/10.57780/esa-tgmpwum.
19. W. T. Thompson, Coordinate systems for solar image data. *Astron. Astrophys.* **449**, 791–803 (2006). doi:10.1051/0004-6361:20054262
20. S. Gosain, P. Venkatakrishnan, The evolution of the twist shear and dip shear during X-class flare of 2006 December 13: Hinode observations. *Astrophys. J. Lett.* **720**, L137–L143 (2010). doi:10.1088/2041-8205/720/2/L137

21. S. Parenti, Solar prominences: Observations. *Living Rev. Sol. Phys.* **11**, 1–88 (2014). doi:10.12942/lrsp-2014-1
22. R. Liu, B. Kliem, V. S. Titov, J. Chen, Y. Wang, H. Wang, C. Liu, Y. Xu, T. Wiegelmann, Structure, stability, and evolution of magnetic flux ropes from the perspective of magnetic twist. *Astrophys. J.* **818**, 148 (2016). doi:10.3847/0004-637X/818/2/148
23. G. H. Fisher, B. T. Welsch, W. P. Abbett, D. J. Bercik, Estimating electric fields from vector magnetogram sequences. *Astrophys. J.* **715**, 242–259 (2010). doi:10.1088/0004-637X/715/1/242
24. M. C. M. Cheung, M. L. DeRosa, A method for data-driven simulations of evolving solar active regions. *Astrophys. J.* **757**, 147 (2012). doi:10.1088/0004-637X/757/2/147
25. A. R. Yeates, Sparse reconstruction of electric fields from radial magnetic data. *Astrophys. J.* **836**, 131 (2017). doi:10.3847/1538-4357/aa5c84
26. E. Lumme, J. Pomoell, E. K. J. Kilpua, Optimization of photospheric electric field estimates for accurate retrieval of total magnetic energy injection. *Sol. Phys.* **292**, 191 (2017). doi:10.1007/s11207-017-1214-0
27. R. Lionello, C. Downs, E. I. Mason, J. A. Linker, R. M. Caplan, P. Riley, V. S. Titov, M. L. DeRosa, Global MHD simulations of the time-dependent corona. *Astrophys. J.* **959**, 77 (2023). doi:10.3847/1538-4357/ad00be
28. C. J. Schrijver, M. L. DeRosa, Photospheric and heliospheric magnetic fields. *Sol. Phys.* **212**, 165–200 (2003). doi:10.1023/A:1022908504100
29. E. I. Mason, R. Lionello, C. Downs, J. A. Linker, R. M. Caplan, M. L. DeRosa, Time-dependent dynamics of the corona. *Astrophys. J. Lett.* **959**, L4 (2023). doi:10.3847/2041-8213/ad00bd
30. Predictive Science, *Live Coronal Prediction: April 8, 2024 Total Solar Eclipse* (2024); https://www.predsci.com/eclipse2024.
31. P. Antolin, C. Froment, Multi-scale variability of coronal loops set by thermal non-equilibrium and instability as a probe for coronal heating. *Front. Astron. Space Sci.* **9**, 820116 (2022). doi:10.3389/fspas.2022.820116
32. Y. Mok, Z. Mikić, R. Lionello, C. Downs, J. A. Linker, A three-dimensional model of Active Region 7986: Comparison of simulations with observations. *Astrophys. J.* **817**, 15 (2016). doi:10.3847/0004-637X/817/1/15
33. S. K. Antiochos, Z. Mikić, V. S. Titov, R. Lionello, J. A. Linker, A model for the sources of the slow solar wind. *Astrophys. J.* **731**, 112 (2011). doi:10.1088/0004-637X/731/2/112
34. Y. M. Wang, N. R. Sheeley Jr., N. B. Rich, Coronal pseudostreamers. *Astrophys. J.* **658**, 1340–1348 (2007). doi:10.1086/511416
35. V. S. Titov, Generalized squashing factors for covariant description of magnetic connectivity in the solar corona. *Astrophys. J.* **660**, 863–873 (2007). doi:10.1086/512671
36. V. S. Titov, Z. Mikić, J. A. Linker, R. Lionello, S. K. Antiochos, Magnetic topology of coronal hole linkages. *Astrophys. J.* **731**, 111 (2011). doi:10.1088/0004-637X/731/2/111
37. S. R. Habbal, M. Druckmüller, N. Alzate, A. Ding, J. Johnson, P. Starha, J. Hoderova, B. Boe, S. Constantinou, M. Arndt, Identifying the coronal source regions of solar wind streams from total solar eclipse observations and in situ measurements extending over a solar cycle. *Astrophys. J. Lett.* **911**, L4 (2021). doi:10.3847/2041-8213/abe775
38. B. Boe, S. Habbal, C. Downs, M. Druckmüller, The solar minimum eclipse of 2019 July 2. II. The first absolute brightness measurements and MHD model predictions of Fe X, XI, and XIV out to 3.4 $R_\odot$. *Astrophys. J.* **935**, 173 (2022). doi:10.3847/1538-4357/ac8101
39. A. R. Yeates, D. H. Mackay, Initiation of coronal mass ejections in a global evolution model. *Astrophys. J.* **699**, 1024–1037 (2009). doi:10.1088/0004-637X/699/2/1024
40. A. R. Yeates, The Sun's non-potential corona over solar cycle 24. *Sol. Phys.* **299**, 83 (2024). doi:10.1007/s11207-024-02328-5
41. J. Newkirk, R. G. Dupree, E. J. Schmhl, Magnetic fields and the structure of the solar corona. II: Observations of the 12 November 1966 solar corona. *Sol. Phys.* **15**, 15–39 (1970). doi:10.1007/BF00149469
42. F. Auchère, E. Soubrié, G. Pelouze, É. Buchlin, Image enhancement with wavelet-optimized whitening. *Astron. Astrophys.* **670**, A66 (2023). doi:10.1051/0004-6361/202245345
43. E. Kalnay, *Atmospheric Modeling, Data Assimilation and Predictability* (Cambridge Univ. Press, 2002).
44. R. Caplan *et al.*, HipFT sample input dataset for convective flows and data assimilation, version 2. Zenodo (2024); https://doi.org/10.5281/zenodo.11205509.
45. C. Downs, A near-real-time data-assimilative model of the solar corona, version 1.0.0. Zenodo (2025); https://doi.org/10.5281/zenodo.14889337.
46. R. Caplan, C. Downs, J. Linker, Z. Mikic, POT3D, version 3.1.0r. Zenodo (2021); https://doi.org/10.5281/zenodo.4690005.
47. R. Caplan *et al.*, HipFT: High-performance Flux Transport, version 1.14.1. Zenodo (2025); https://doi.org/10.5281/zenodo.14942123.
48. J. A. Linker, T. Torok, C. Downs, R. M. Caplan, V. Titov, A. Reyes, R. Lionello, P. Riley, CORHEL-CME: An interactive tool for modeling solar eruptions. *J. Phys. Conf. Ser.* **2742**, 012012 (2024). doi:10.1088/1742-6596/2742/1/012012
49. Joint Science Operations Center, HMI near real time quick-look magnetograms with a cadence of 720 seconds (record hmi.m_720s_nrt); http://jsoc.stanford.edu/ajax/lookdata.html?ds=hmi.m_720s_nrt.
50. Joint Science Operations Center (JSOC); http://jsoc.stanford.edu.
51. T. R. Metcalf, K. D. Leka, G. Barnes, B. W. Lites, M. K. Georgoulis, A. A. Pevtsov, K. S. Balasubramaniam, G. A. Gary, J. Jing, J. Li, Y. Liu, H. N. Wang, V. Abramenko, V. Yurchyshyn, Y.-J. Moon, An overview of existing algorithms for resolving the 180° ambiguity in vector magnetic fields: Quantitative tests with synthetic data. *Sol. Phys.* **237**, 267–296 (2006). doi:10.1007/s11207-006-0170-x
52. Y. M. Wang, N. R. Sheeley Jr., On potential field models of the solar corona. *Astrophys. J.* **392**, 310 (1992). doi:10.1086/171430
53. J. T. Hoeksema, Y. Liu, K. Hayashi, X. Sun, J. Schou, S. Couvidat, A. Norton, M. Bobra, R. Centeno, K. D. Leka, G. Barnes, M. Turmon, The Helioseismic and Magnetic Imager (HMI) vector magnetic field pipeline: Overview and performance. *Sol. Phys.* **289**, 3483–3530 (2014). doi:10.1007/s11207-014-0516-8
54. P. W. Schuck, S. K. Antiochos, K. D. Leka, G. Barnes, Achieving consistent Doppler measurements from SDO/HMI vector field inversions. *Astrophys. J.* **823**, 101 (2016). doi:10.3847/0004-637X/823/2/101
55. L. Upton, D. H. Hathaway, Predicting the Sun's polar magnetic fields with a surface flux transport model. *Astrophys. J.* **780**, 5 (2014). doi:10.1088/0004-637X/780/1/5
56. D. Nandy, P. Bhowmik, A. R. Yeates, S. Panda, R. Tarafder, S. Dash, The large-scale coronal structure of the 2017 August 21 great american eclipse: An assessment of solar surface flux transport model enabled predictions and observations. *Astrophys. J.* **853**, 72 (2018). doi:10.3847/1538-4357/aaa1eb
57. N. V. Pogorelov, C. N. Arge, R. M. Caplan, P. Colella, J. A. Linker, T. Singh, B. Van Straalen, L. Upton, C. Downs, C. Gebhart, D. V. Hegde, C. Henney, S. Jones, C. Johnston, T. K. Kim, A. Marble, S. Raza, M. M. Stulajter, J. Turtle, Space Weather with Quantified Uncertainties: Improving Space Weather Predictions with Data-Driven Models of the Solar Atmosphere and Inner Heliosphere. *J. Phys. Conf. Ser.* **2742**, 012013 (2024). doi:10.1088/1742-6596/2742/1/012013
58. J. Worden, J. Harvey, An evolving synoptic magnetic flux map and implications for the distribution of photospheric magnetic flux. *Sol. Phys.* **195**, 247–268 (2000). doi:10.1023/A:1005272502885
59. C. N. Arge *et al.*, *Am. Inst. Phys. Conf. Series* **1539**, 11–14 (2013).
60. D. H. Hathaway, L. A. Upton, S. S. Mahajan, Variations in differential rotation and meridional flow within the Sun's surface shear layer 1996–2022. *Front. Astron. Space Sci.* **9**, 1007290 (2022). doi:10.3389/fspas.2022.1007290
61. D. H. Hathaway, P. E. Williams, K. Dela Rosa, M. Cuntz, The advection of supergranules by the Sun's axisymmetric flows. *Astrophys. J.* **725**, 1082–1090 (2010). doi:10.1088/0004-637X/725/1/1082
62. C. J. Schrijver, A. M. Title, A. A. van Ballegooijen, H. J. Hagenaar, R. A. Shine, Sustaining the quiet photospheric network: The balance of flux emergence, fragmentation, merging, and cancellation. *Astrophys. J.* **487**, 424–436 (1997). doi:10.1086/304581
63. Joint Science Operations Center, HMI pole filled synoptic map for CR 2279; http://jsoc.stanford.edu/ajax/exportdata.html?ds=hmi.synoptic_mr_polfil_720s%5B2279%5D.
64. Predictive Science, MAS: A model of the solar corona and inner heliosphere; https://www.predsci.com/mas.

65. R. Lionello, Z. Mikić, J. A. Linker, Stability of algorithms for waves with large flows. *J. Comput. Phys.* **152**, 346–358 (1999). doi:10.1006/jcph.1999.6250
66. J. A. Linker, S. G. Heinemann, M. Temmer, M. J. Owens, R. M. Caplan, C. N. Arge, E. Asvestari, V. Delouille, C. Downs, S. J. Hofmeister, I. C. Jebaraj, M. S. Madjarska, R. F. Pinto, J. Pomoell, E. Samara, C. Scolini, B. Vršnak, Coronal hole detection and open magnetic flux. *Astrophys. J.* **918**, 21 (2021). doi:10.3847/1538-4357/ac090a
67. R. Lionello, M. Velli, C. Downs, J. A. Linker, Z. Mikić, A. Verdini, Validating a time-dependent turbulence-driven model of the solar wind. *Astrophys. J.* **784**, 120 (2014). doi:10.1088/0004-637X/784/2/120
68. C. Downs, R. Lionello, Z. Mikić, J. A. Linker, M. Velli, Closed-field coronal heating driven by wave turbulence. *Astrophys. J.* **832**, 180 (2016). doi:10.3847/0004-637X/832/2/180
69. T. Török, C. Downs, J. A. Linker, R. Lionello, V. S. Titov, Z. Mikić, P. Riley, R. M. Caplan, J. Wijaya, Sun-to-Earth MHD simulation of the 2000 July 14 Bastille Day eruption. *Astrophys. J.* **856**, 75 (2018). doi:10.3847/1538-4357/aab36d Medline
70. Y. Liu, J. T. Hoeksema, P. H. Scherrer, J. Schou, S. Couvidat, R. I. Bush, T. L. Duvall Jr., K. Hayashi, X. Sun, X. Zhao, Comparison of line-of-sight magnetograms taken by the Solar Dynamics Observatory/Helioseismic and Magnetic Imager and Solar and Heliospheric Observatory/Michelson Doppler Imager. *Sol. Phys.* **279**, 295–316 (2012). doi:10.1007/s11207-012-9976-x
71. M. Weinzierl, A. R. Yeates, D. H. Mackay, C. J. Henney, C. N. Arge, A new technique for the photospheric driving of non-potential solar coronal magnetic field simulations. *Astrophys. J.* **823**, 55 (2016). doi:10.3847/0004-637X/823/1/55
72. S. H. B. Livi, S. Martin, H. Wang, G. Ai, The association of flares to cancelling magnetic features on the sun. *Sol. Phys.* **121**, 197–214 (1989). doi:10.1007/BF00161696
73. A. R. Yeates, T. Amari, I. Contopoulos, X. Feng, D. H. Mackay, Z. Mikić, T. Wiegelmann, J. Hutton, C. A. Lowder, H. Morgan, G. Petrie, L. A. Rachmeler, L. A. Upton, A. Canou, P. Chopin, C. Downs, M. Druckmüller, J. A. Linker, D. B. Seaton, T. Török, Global non-potential magnetic models of the solar corona during the March 2015 eclipse. *Space Sci. Rev.* **214**, 99 (2018). doi:10.1007/s11214-018-0534-1 Medline
74. R. M. Caplan, C. Downs, J. A. Linker, Z. Mikic, Variations in finite-difference potential fields. *Astrophys. J.* **915**, 44 (2021). doi:10.3847/1538-4357/abfd2f
75. S. F. Martin, Conditions for the formation and maintenance of filaments (invited review). *Sol. Phys.* **182**, 107–137 (1998). doi:10.1023/A:1005026814076
76. A. A. Pevtsov, K. S. Balasubramaniam, J. W. Rogers, Chirality of chromospheric filaments. *Astrophys. J.* **595**, 500–505 (2003). doi:10.1086/377339
77. S. K. Antiochos, Helicity condensation as the origin of coronal and solar wind structure. *Astrophys. J.* **772**, 72 (2013). doi:10.1088/0004-637X/772/1/72
78. G. Del Zanna, K. P. Dere, P. R. Young, E. Landi, CHIANTI—An atomic database for emission lines. XVI. Version 10, further extensions. *Astrophys. J.* **909**, 38 (2021). doi:10.3847/1538-4357/abd8ce
79. J. T. Schmelz, D. V. Reames, R. von Steiger, S. Basu, Composition of the solar corona, solar wind, and solar energetic particles. *Astrophys. J.* **755**, 33 (2012). doi:10.1088/0004-637X/755/1/33
80. NASA Solar Dynamics Observatory Atmospheric Imaging Assembly, Instrumental response data from the "sdo/aia" SolarSoft IDL package; https://hesperia.gsfc.nasa.gov/ssw/sdo/aia/response.
81. T. A. Howard, S. J. Tappin, Interplanetary coronal mass ejections observed in the heliosphere: 1. Review of theory. *Space Sci. Rev.* **147**, 31–54 (2009). doi:10.1007/s11214-009-9542-5

ACKNOWLEDGMENTS

We thank the NASA Advanced Supercomputing Division (NAS) for allocations on the Pleiades, Electra, and Aitken supercomputers and the NSF ACCESS program for allocations on the Expanse supercomputer at the San Diego Supercomputer Center (SDSC), which were used to run the simulations. These simulations would not have been possible without the generous support from personnel at both centers, as well as the use of special priority queues. We thank the SDO/HMI team of the Solar Physics Group at Stanford University for providing timely access to HMI Synoptic magnetograph data. We thank D. H. Hathaway for providing the code on which ConFlow was built. We thank J. Zhang for facilitating access to the eclipse image in Fig. 4B and Y. Li, Q. Lao, B. Wang, and Y. Huang for assistance in processing it. Solar Orbiter is a space mission of international collaboration between ESA and NASA, operated by ESA. We are grateful to the ESA SOC and MOC teams for their support. The Solar Orbiter project received funding from the European Research Council (ERC) under the European Union's Horizon 2020 research and innovation program (grant agreement 101097844—project WINSUN). The German contribution to Solar Orbiter/PHI is funded by the BMWi through DLR and by MPG central funds. The Spanish contribution is funded by AEI/MCIN/10.13039/501100011033 and European Union "Next-GenerationEU/PRTR" (RTI2018-096886-C5, PID2021-1253250B-C5, PCI2022-135009-2, and PCI2022-135029-2) and ERDF "A way of making Europe" and "Center of Excellence Severo Ochoa" awards to Instituto de Astrofísica de Andalucía–Consejo Superior de Investigaciones Científicas (SEV-2017-0709 and CEX2021-001131-S). The French contribution was funded by CNES. The views expressed are those of the authors and do not reflect the official guidance or position of the US government, the Department of Defense, or the US Air Force. **Funding:** C.D, J.A.L., R.M.C., E.I.M, P.R., R.D., A.R., E.P., R.L., J.T., M.B.-N., M.M.S., V.S.T., and T.T. were supported by NASA grants (80NSSC20K1285, 80NSSC18K1129, 80NSSC22K1021, 80NSSC20K0192, 80NSSC20K1274, 80NSSC19K0858, and 80NSSC22K0893) and NSF grants (ICE-1854790 and AGS-1923377), by SwRI from NASA grant 80NSSC22K0523, and by the Naval Research Laboratory under subcontract N00173-19-C-2003 (Wide-field Imager for Parker Solar Probe and The Solar Orbiter Heliospheric Imager, from NASA contract NNG11EK11I), and by Johns Hopkins Applied Physics Laboratory from NASA grant 80NSSC21K1860. L.A.U. and B.K.J. were also supported by NASA grant 80NSSC22K0893. J.A.L., R.M.C, C.D, J.T., L.A.U., R.A., B.K.J., and C.N.A. were supported by the University of Alabama from the NSF/NASA SWQU program (grants AGS 2028154 and 80NSSC20K1582). C.N.A. was supported by the NASA Heliophysics Internal Scientist Funding Model (ISFM). C.J.H. was supported by the Air Force Office of Scientific Research task 22RVCOR012. X.C. and S.W. were supported by NSFC under grant 12333009. D.O.S. was funded by a Ramon y Cajal fellowship. **Author contributions:** C.D. led the project, developed the preprocessing pipeline, prepared and assimilated the magnetic data, developed the visualization pipeline, and ran the MHD model. J.A.L., P.R., and C.D. wrote the manuscript. R.M.C. led the development of HipFT, with contributions from M.M.S., J.A.L, C.D., L.A.U, B.K.J., R.A., C.N.A., and C.J.H.; J.T. and C.D. developed the HMI acquisition and mapping pipeline. C.D. and E.I.M. developed the energization component. R.D. and A.R. developed the prediction website (*30*), with content provided by J.A.L., P.R., C.D., and E.P.; E.P. assisted with coronagraph visualizations. R.L., E.I.M., M.B.-N., V.S.T., and T.T assisted with the MHD model. H.S., D.O.S., and J.B.R. developed the PHI data processing software. D.G. and G.V. performed the real-time PHI data processing. J.H., D.C., and S.K.S. implemented the SolO observation programs. X.C. and S.W. provided the eclipse image for comparison. All co-authors reviewed the manuscript. **Competing interests:** L.A.U. is a member of NASA's Heliophysics Advisory Committee. All other authors declare no competing interests. **Data and materials availability:** The HMI and PHI data were taken from public archives, as described in the supplementary materials. All 40,000 synthetic observable images and corresponding animations are available on the project website (*30*) under "Science Data." The ConFlow (*14*) output is archived at Zenodo (*44*). The HipFT output is archived at Zenodo (*45*). The SFT model input and output, MHD input and simulation snapshots, and the synthetic images used to create the figures are also archived at Zenodo (*45*). The Pot3D code is available at https://github.com/predsci/POT3D and archived at Zenodo (*46*). The HipFT code is available at https://github.com/predsci/HipFT and archived at Zenodo

(*47*). The version of the Mas code used in this study is archived at Zenodo (*45*). A similar version of Mas is available to run on request at NASA's Community Coordinated Modeling Center https://ccmc.gsfc.nasa.gov/models by searching for "CORHEL-CME" (*48*).

SUPPLEMENTARY MATERIALS

science.org/doi/10.1126/science.adq0872
Materials and Methods
Figs. S1 to S8
References (*49*–*81*)
Movies S1 to S9

Submitted 3 May 2024; accepted 25 April 2025
Published online 10 June 2025
10.1126/science.adq0872

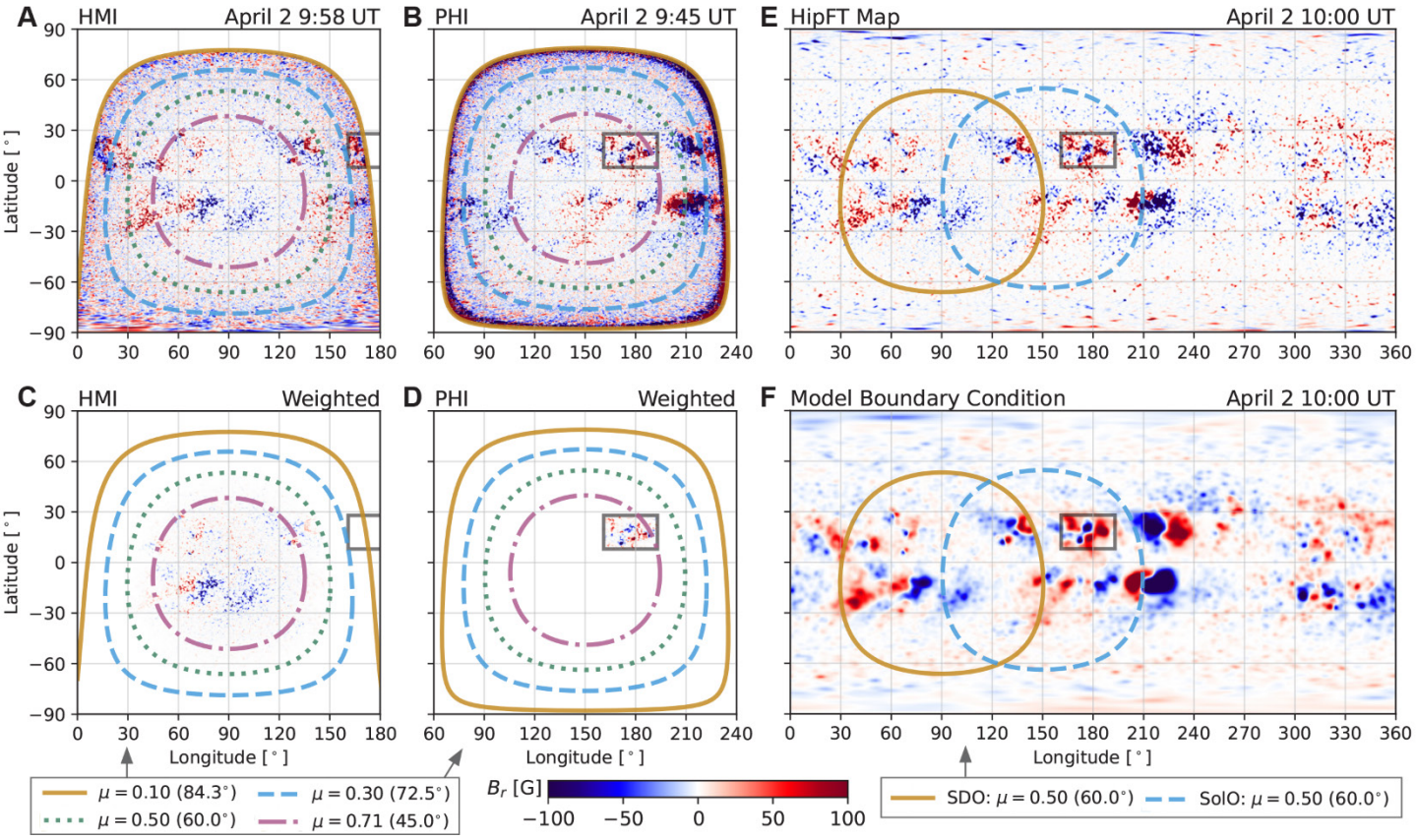

Fig. 1. Input data, assimilation, and modeling of solar photospheric magnetic fields. (**A** and **B**) Maps of B_r in gauss (color bar) from (A) HMI and (B) PHI, in Carrington coordinates, for an example timestep near 2 April 2024 10:00 UT. Contours indicate values of μ (bottom left legend). The gray rectangles indicate the assimilation region for PHI (*14*); it encloses an AR complex that is at the edge of the HMI field of view but well observed with PHI. (**C**) The HMI data after weighting by μ^4, ready for assimilation. (**D**) The PHI data after uniform weighting within the enclosed AR complex only. (**E**) The global B_r map predicted by HipFT after assimilation. Contours show the μ = 0.5 (60°) regions for both SDO and SolO, to indicate their respective viewpoints. (**F**) Same as (E), but for the derived B_r boundary condition of the MHD model. Animated versions of (A) and (C) are shown in movie S1, and animated versions of (E) and (F) are shown in movie S2, for the entire simulation.

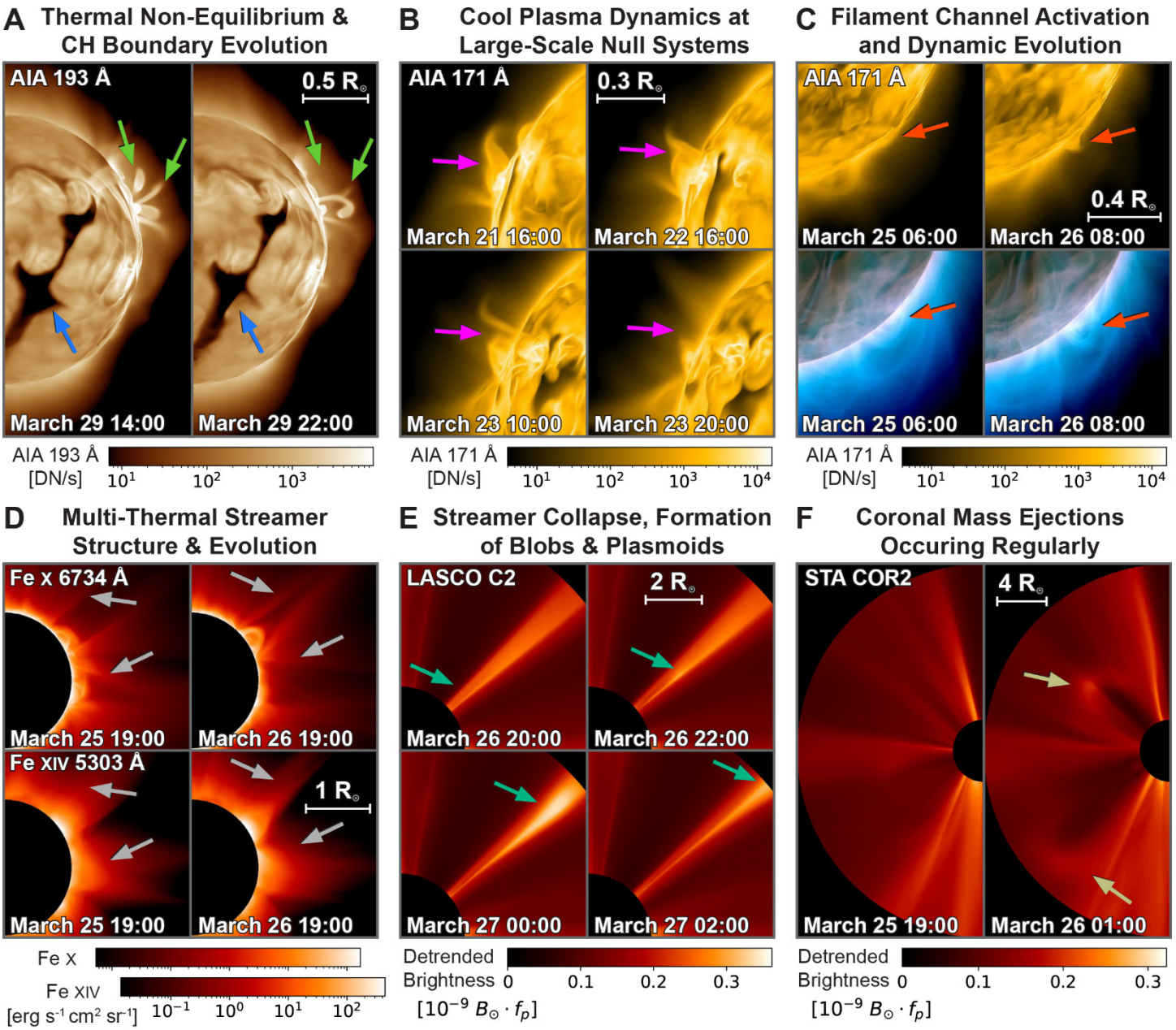

Fig. 2. Dynamic features in the synthetic observables from the time-evolving model. (**A**) Synthetic AIA 193 Å images, showing thermal nonequilibrium (green arrows) and CH boundary evolution (blue arrows). The color bar is in data numbers per second (DN/s), and $R_\odot$ is the solar radius. (**B**) Synthetic AIA 171 Å images, showing cool material evolving above a low-lying pseudostreamer null point (magenta arrows). (**C**) (Top) Synthetic AIA 171 Å image and (bottom) tricolor volume rendered (*14*) *Q* (*6*), showing cool material collecting in a filament channel (red arrows). (**D**) Synthetic Fe x 6734 Å and Fe xiv 5303 Å emission line intensities, showing multithermal structure and evolution of streamers (gray arrows). (**E**) Synthetic LASCO-C2 coronagraph images, showing the formation and ejection of a streamer blob (teal arrows). The color bar shows the product of $B_\odot$, the brightness at the center of the solar disk, and the detrending function f_p (fig. S8) (*14*). (**F**) Synthetic STEREO-A (STA) COR2 coronagraph images, showing a CME (gold arrows). Corresponding animations of (A) to (F) are shown in movies S4 to S9, respectively.

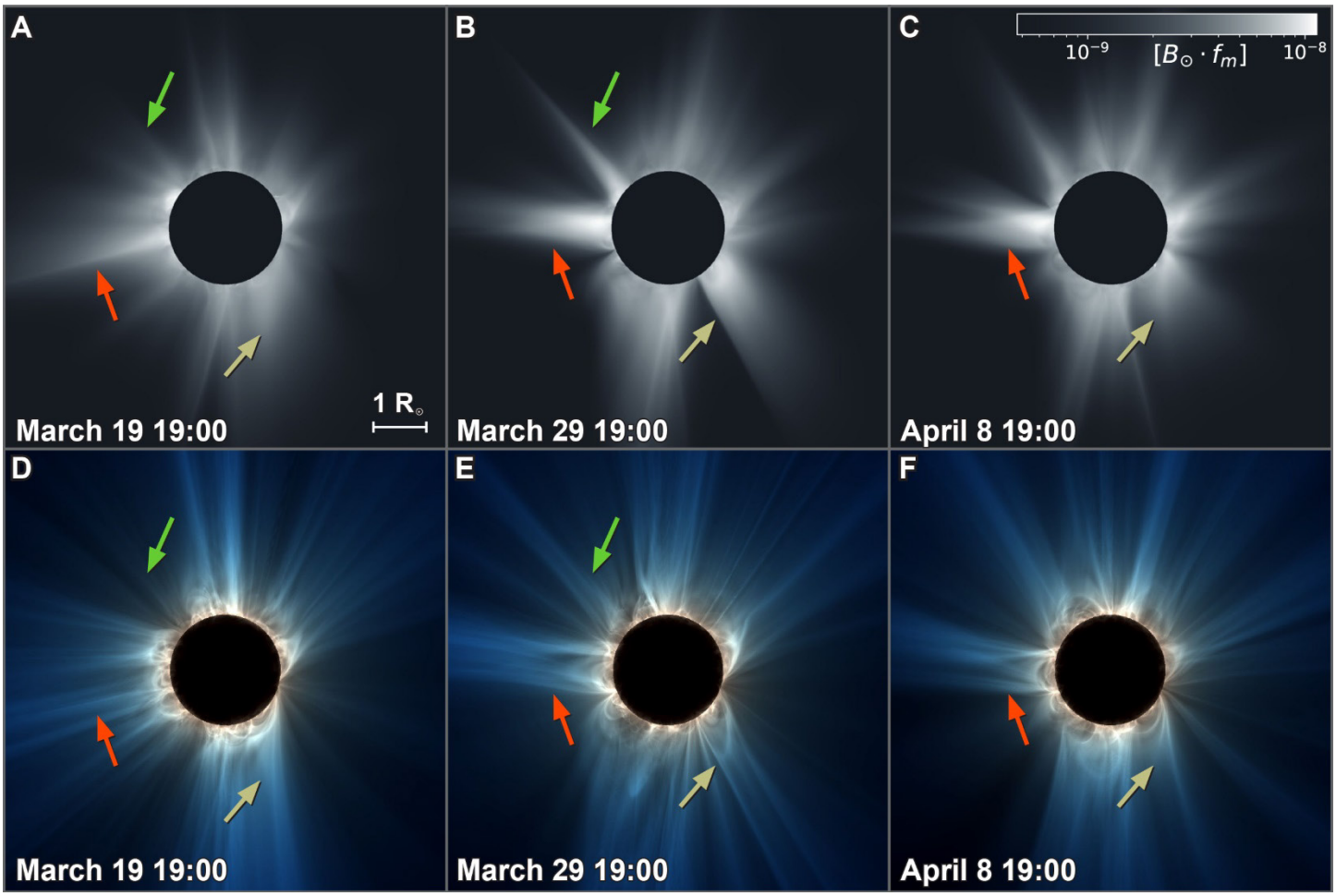

Fig. 3. Time evolution of the prediction over several weeks. Shown are the predicted view from Earth for the time of the eclipse (8 April 2024 18:42 UT). Solar north is up. (**A** to **C**) Detrended white-light brightness predicted at three different times (labeled) during the simulation. (**D** to **F**) Volume-rendering of Q (*6*), which highlights magnetic structure. Sets of colored arrows indicate streamer structures that change position over time. An animation of the predictions over the entire simulation period is shown in movie S3.

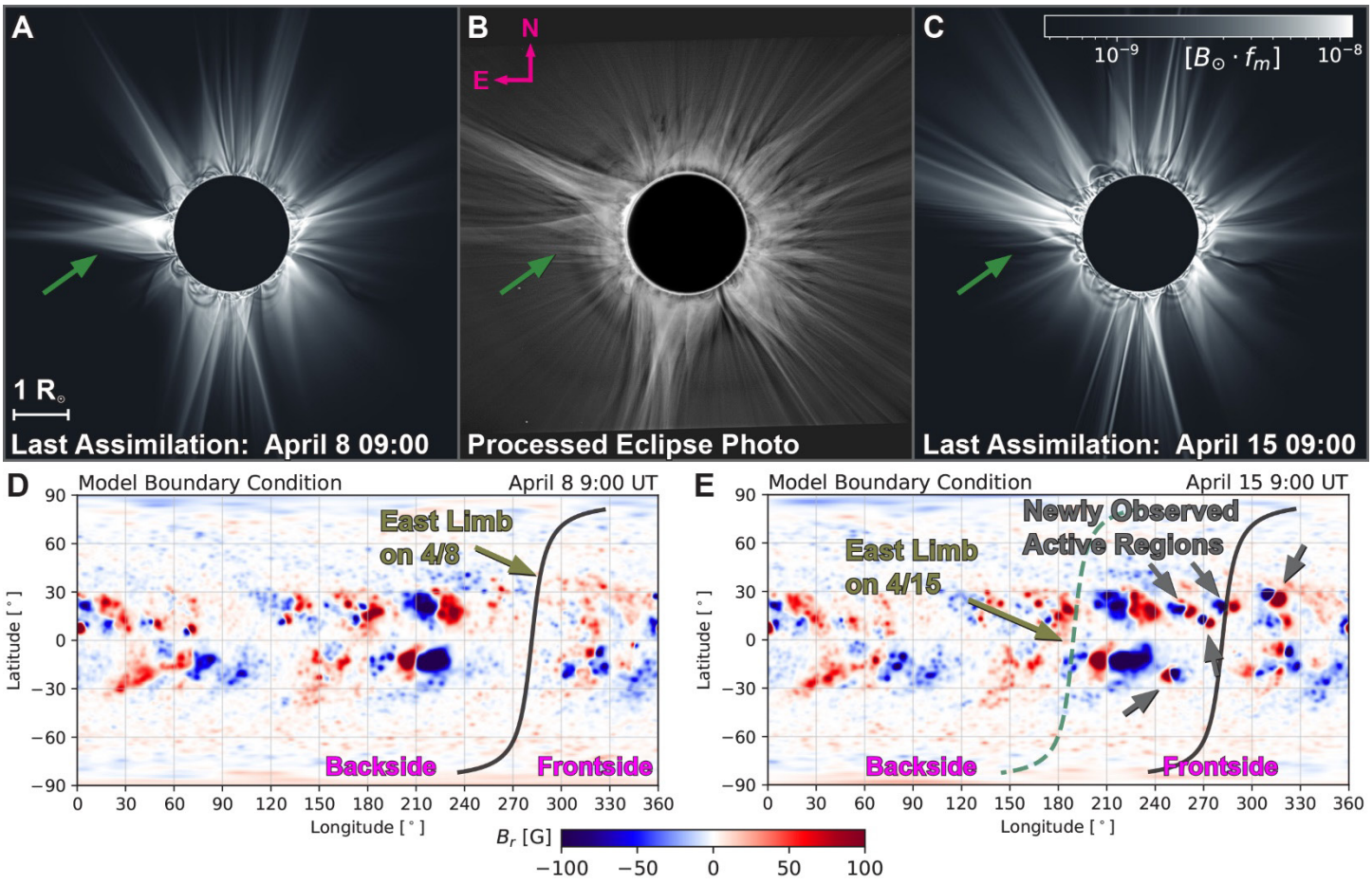

Fig. 4. Comparison between the predicted and observed corona during the eclipse. (**A**) Wavelet sharpened and detrended brightness from the model prediction made at 8 April 2024 9:00 UT. (**B**) Composite eclipse photo processed (*14*) to highlight coronal structures observed during totality. (**C**) Same as (A), but after an additional week of data assimilation. f_m is an alternative detrending function (fig. S8) (*14*). The streamer on the northeast limb (green arrows) shifts position between the two predictions, owing to the emergence of several new ARs. The evolution of the sharpened brightness is shown in movie S3, middle. (**D**) Similar to Fig. 1F, but for the boundary condition at 8 April 2024 9:00UT. The position of the east limb during the eclipse (solid line) is indicated. (**E**) Same as (D) but 1 week later, corresponding to (C). Gray arrows indicate ARs that were not present in (D).